SISSA

PAPER • OPEN ACCESS

Fast forward modeling of neutral beam injection and halo formation including full Balmer-α emission prediction at W7-X

To cite this article: S. Bannmann *et al* 2023 *JINST* **18** P10029

View the article online for updates and enhancements.

Fast forward modeling of neutral beam injection and halo formation including full Balmer-α emission prediction at W7-X

S. Bannmann,[*] **O. Ford, U. Hoefel, P. Poloskei, A. Pavone, S. Kwak, J. Svensson, S. Lazerson, P. McNeely, N. Rust, D. Hartmann, E. Pasch, G. Fuchert, R.C. Wolf and the W7-X-Team**[1]

Max-Planck-Institut für Plasmaphysik,
Wendelsteinstr. 1, 17491 Greifswald, Germany

E-mail: sebastian.bannmann@ipp.mpg.de

ABSTRACT: A full collisional-radiative (CR) neutral beam injection model based on Gaussian pencil (Gausscil) beams and a diffusive CR neutral halo model are presented. The halo is a neutral cloud around the neutral beam forming due to multiple charge exchange (CX) reactions. Both models do not rely on Monte-Carlo techniques and are thereby orders of magnitude faster than commonly used models. To model the neutral halo a system of coupled diffusion equations is solved numerically, enforcing mixed boundary conditions. From the equilibrium hydrogen neutral densities in the second excited energy state (n = 3), the Balmer-α emission intensity is calculated and the full spectrum is predicted, including effects as Doppler shifts and broadening due to the complex neutral beam geometry and the motional Stark effect (MSE) from the magnetic field. All forward models are implemented in the Minerva [1] Bayesian analysis framework to enable detailed multivariant inference from Balmer-α spectroscopy data. The modeled neutral beam and halo densities are successfully verified against calculations with a validated Monte-Carlo code for the W7-X beam and plasma geometry, especially proving the validity of the halo diffusion ansatz. A comparison of the predicted emission spectra with the experimental data proves the accuracy of the implemented model. All important parameters defining the neutral beams are inferred and compared to available reference values.

---

[1]See Pedersen et al. 2022 (https://dx.doi.org/10.1088/1741-4326/ac2cf5) for the W7-X Team author list.
[*]Corresponding author.

Contents

1   Introduction

Neutral beam injection (NBI) of hydrogen or deuterium is a common plasma heating technique at fusion experiments world wide, including at Wendelstein 7-X (W7-X) [2]. Additionally, neutral beam spectroscopy offers a high diagnostic value [3]. The measured spectra are sensitive to all NBI parameters (total beam power, species fraction, beam positioning in space and beamlet divergence)[1] and the electron density profile. By setting up a sophisticated beam model one can use Bayesian inference to fit all of these physical parameters simultaneously. This can help to resolve uncertainties of the vertical beam position and injected power. Obtaining precise beam parameters not only serves as a verification of the neutral beam injection system parameters but also is one of several important factors in detailed main ion power and particle transport studies in NBI heated plasmas. The beam fueling profile which is determining the particle source function in the plasma volume is sensitive to all NBI parameters. The accuracy with which electron density profiles can be obtained from the data will be worthwhile to assess, as this would provide an independent source of absolute electron densities, currently only provided at W7-X by the Thomson Scattering diagnostic, normalised to a single line interferometer.

---

[1]Defined as the angle from the beamlet axis to the cone edge with a radius of one σ in a Gaussian beamlet shape.

When penetrating the plasma, neutral beam particles can be energetically excited through electron and ion collisions and subsequently emit light. A particular bright and easy to measure line is the Balmer-α line ($\lambda = 656.28$ nm) which represents the n = 3 to n = 2 transition in hydrogen. Active beam emission spectroscopy (BES) allows measurements of beam and/or plasma parameters localised to the intersection of the diagnostic line of sight and the beam. At W7-X, some proof of principle BES measurements and their preliminary analysis are described in [4]. It could be seen that a simple multi-Gaussian fitting of the emission spectra is not sufficient for a routine analysis due to the high number of parameters influencing the shape and the magnitude of the BES signal. It was concluded that, in order to extract all the information possible from the active Balmer-α emission spectra, an accurate and consistent forward model of the neutral beam attenuation and emission is needed. In section 2 of this paper the NBI model implemented in the Minerva framework [1] is described. Special emphasis is laid on the newly implemented quasi time dependent collisional-radiative model of the beam injection, enabling the prediction of the beam emission at the very plasma edge.

Charge-exchange (CX) reactions between the penetrating beam and the surrounding thermal plasma not only ionize the beam but also serve as the source function of a new neutral species, the so-called halo. It consists of CX neutralized main plasma ions and is therefore a thermal neutral species. Halo particles will on average undergo several CX reactions before they are finally ionized by ion or electron impact ionization processes. Equivalent to the neutral beam particles, halo particles can be excited and emit light before they are ionized. Computationally, the halo formation and emission is not trivial to model due to the complex combination of diffusive transport processes, spatially varying source terms and collisional-radiative processes. A viable but also costly solution is employing a Monte-Carlo technique as is done in the FIDASIM code [5, 6]. In section 3, a newly implemented halo model is presented. It relies on a CX diffusion Ansatz combined with collisional-radiative (CR) modeling of up to 5 excited states to be able to predict the light emission. It is several orders of magnitude faster than Monte-Carlo codes which makes it feasible to be used in Bayesian inference calculations, as these require many repeated model evaluations in order to explore the space of input parameters.

A simplified diffusive halo model was used in [7] as initial verification of FIDASIM calculations. The modeled beam and halo densities in several energy states are benchmarked against FIDASIM as presented in section 4.

The full Balmer-α emission spectrum has a complex shape being the superposition of halo, beam and passive emission components as sketched in figure 1. The beam emission signal is Doppler shifted in the spectrum proportionally to the viewing angle and the velocity of the beam particles. Due to the acceleration of not only H^+ but also H_2^+ and H_3^+ the beam consists of 3 H_0 species with different injection energies (E, E/2, E/3). Each of these components has a different Doppler shift and is split into several lines due to the motional Stark effect (MSE) [8], which is explained in detail in section 5. There is a slight Doppler broadening of each line according to the beam divergence. The halo emission is Doppler broadened proportionally to the main ion temperature and in principle Doppler shifted by the bulk plasma velocity (<10 km/s [4]). The emission from recycling hydrogen is localized at the divertor and the plasma edge and has a small Doppler broadening compared to the halo emission due to the low temperature of the hydrogen neutrals.
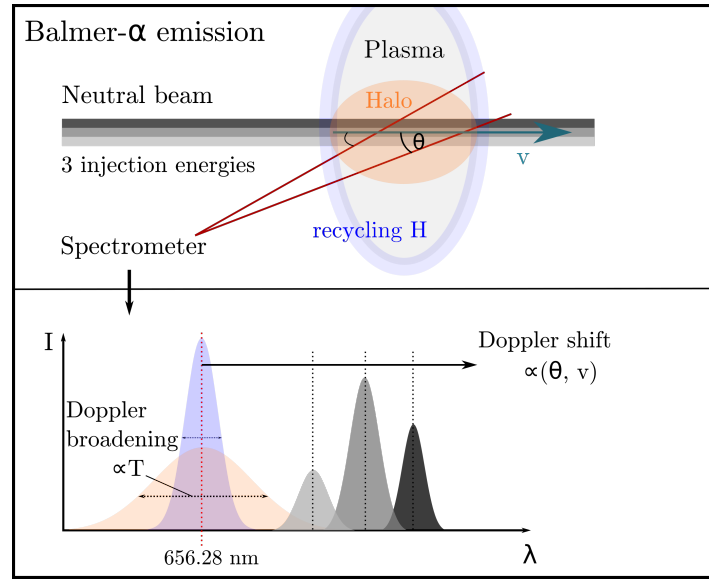
Figure 1. Constituents of a Balmer-α beam emission spectrum (bottom) from different physical and geometrical contributions (top) including Doppler shifted beam emission (black/gray), halo (orange) and cold recycled hydrogen (blue). A single injected neutral hydrogen beam consists of particles with 3 different kinetic energies (shown in gray tones).

Fusion experiments world wide employ beam emission spectroscopy as a plasma physics diagnostic and rely on accompanying modeling tools. At DIIID, a fitting toolchain employing FIDASIM is used to fit the main ion (deuterium) temperature, density and rotation from beam spectroscopy data [9]. The main time consuming calculation is the FIDASIM run. At ASDEX upgrade, the CHICA code [10] is capable to model the beam and halo on different levels of accuracy and speed. The fast, full collisional-radiative model relies on a Gaussian beam shape description and models the halo perpendicular to the beam axis using ionization and charge-exchange fall-off lengths. At W7-X, a validated Monte-Carlo code (BEAMS3D) [11] is used, among other purposes, to calculate the beam deposition.

In this paper an alternative beam and halo model is presented. It is implemented in the Minerva Bayesian analysis framework. It does not rely in any step on Monte-Carlo techniques and is thereby deterministic and fast compared to other codes. The implemented model is verified against FIDASIM at W7-X relevant parameters. The inference of NBI parameters from full Balmer-α spectra and comparing them to the nominal values serve as a model validation.

2 Neutral beam injection model

Each NBI source consists of a plasma ion source behind an accelerating grid. At W7-X, the grid is spatially extended (H$\times$ W: $50.6 \, \text{cm} \times 22.8 \, \text{cm}$) and has $\approx$800 small holes, each creating a small 'beamlet' of accelerated particles. As not only hydrogen but also single charged H_2^+ and H_3^+ are accelerated, the beam injected into the plasma consists of 3 energy species of H_0, where each species

is carrying a fraction of the total injected power. Each beam is focused through beamlet steering. As the vertical and horizontal beamlet focusing points do not coincide, there exists a horizontal and a vertical focal line at a distance from the source grid of 6.5 m and 8.5 m, respectively. The accelerated ions pass a neutralizer on the way to the plasma. About 8–16%, depending on the installed source, of the neutralized beam is lost (scraped off) on the way to the plasma due to the beam duct and port partly blocking the beam path. When the beam enters the plasma after 7.5 m it has a diameter of roughly 20 cm, which is determined by the beamlet steering and divergence. On the way through the plasma the beam is attenuated by ionizing collisions proportionally to the plasma density seen by the injected neutrals. Due to the beam divergence and the spatial spread of the beam there is a range of actual neutral particle trajectories through the plasma, each encountering different plasma densities and temperatures along its path. Consequently, modeling the beam only along a single beam axis, using a Gaussian function to represent the shape of the beam in the plane perpendicular to the axis, is inaccurate. On the other hand, modeling each beamlet individually would be computationally very expensive. As a balance between both approaches, the grid area is divided into equally spaced Gaussian pencil (Gausscil) beams which are pointed on the vertical and horizontal focal points. Each Gausscil is carrying the same fraction of the total neutral flux. The beam attenuation and the subsequent halo calculation are performed individually for each Gausscil. A typical number of Gausscils used for the calculations in this paper is a 2×5 grid. There are two main reasons for employing such a model. First, the variation of plasma density across the beam cross section can be better captured in the attenuation calculation. Second, the range of angles between beam particle trajectories and an optical line of sight, which leads to a Doppler broadening of the measured beam emission component, can be reproduced.

As shown in table 1, the forward model has a set of basic free parameters determining the beam positioning, shape and species power fraction (fraction of total injected power carried by each of the 3 beam energy species). These need to either be set for a forward run or can be left as free parameters to be fitted via Bayesian inference from Balmer-α beam and halo emission spectroscopy data.

Table 1. NBI paramters at W7-X.

NBI parameter	Nominal value
Source grid: size, position, orientation	W7-X CAD geometry
Horizontal and vertical focal lengths	[6.5, 8.5] m
Beamlet divergence	0.8°
Total power into torus (2 sources active)	(3.1 ± 0.8) MW [12]
Species power fractions	$\approx [0.49, 0.43, 0.08]$

The beamlet divergence is related to the Gausscil divergence via simple trigonometric relations. As the beam duct and especially the duct scrape off losses are not taken care of in this analysis only the beam power injected into the torus can be inferred. The scrape off losses can be modeled with Monte-Carlo codes, as is done by BEAMS3D. A full calorimetric analysis of the beam power flows was done in [12].

2.1 Collisional-radiative model

On the way through the plasma the beam is ionized by electron and ion impact ionization and charge exchange reactions. At the same time beam neutrals are energetically excited by electron and ion impact collisions and deexcited by spontaneous photon emission. These state populating and depopulating collisional-radiative (CR) processes are calculated stepwise along the Gausscil axis and in every step the neutral fluxes in every state are updated accordingly. By exploiting the constant beam particle velocities, the time derivative in the CR calculation can be replaced by a spatial derivative as described in [13]. Let $\boldsymbol{\Phi}$ be the neutral flux vector where each component represents the flux in excitation state i. In a coordinate system where z is the coordinate along the gausscil axis the differential equation governing the evolution of neutral fluxes in several energy states reads the following:

$$\frac{\mathrm{d}\boldsymbol{\Phi}(z)}{\mathrm{d}z} = \frac{1}{v_b}\mathbf{T}_{\mathrm{CR}}\boldsymbol{\Phi}(z) \tag{2.1}$$

Here v_b is the beam particle velocity and $\mathbf{T}_{\mathrm{CR}}$ a matrix containing all CR rates. If one tracks k energy states it is written as

$$T_{\mathrm{CR}} = T_{\mathrm{CR}}(T_e, T_i, n_e) = \begin{bmatrix} -L_1 & A_{21} & A_{31} & . & A_{k1} \\ E_{12} & -L_2 & A_{32} & . & A_{k2} \\ E_{13} & E_{23} & -L_3 & . & . \\ . & . & . & . & A_{ki} \\ E_{1k} & E_{2k} & . & E_{jk} & -L_k \end{bmatrix}. \tag{2.2}$$

Here A are the Einstein coefficients for spontaneous deexcitation, E_{ij} the collisional excitation rates and L_i the summed loss rate to state i. Detailed equations for the excitation rates can be found in the appendix B.

As photonic deexcitation processes happens on the time scale on the order of a few nanoseconds and the fastest beam particles need ≈ 1.8 ms to travel from the neutralizer to the plasma edge, it is valid to assume that the neutralized beam reaches the plasma in the ground state. Only after a certain distance into the plasma is an equilibrium between all neutral beam energy states reached. The penetration depth to reach this equilibrium is shown in the bottom plot of figure 2 and varies from around 10 cm at very low plasma densities (1e18 m^{-3}) to about 2 cm at high densities (3e20 m^{-3}) for a beam energy of 40 keV. A lower beam energy leads to slightly lower values.

The CR model is validated on data from Hutchinson [14] as shown in the top plot of figure 2. For a beam energy of 20 and 40 keV, the equilibrium population fraction in the n = 3 state is computed for a range of electron densities. All plasma profiles are assumed to be flat for this calculation. The obtained population fractions agree very well with the Hutchinson data which is ultimately also a verification of the used FIDASIM cross section data. In simpler analyses (e.g. [4]), precomputed 'beam-emission' and 'beam-stopping' coefficients are used which are generated from a CR-model assuming an infinite homogeneous plasma and it is assumed that all excitation states are already in equilibrium. These are applied to each spatial point individually, leading to significant errors, especially in the emission intensity prediction, for points closer to the plasma edge than the distance (depth) shown in figure 2.
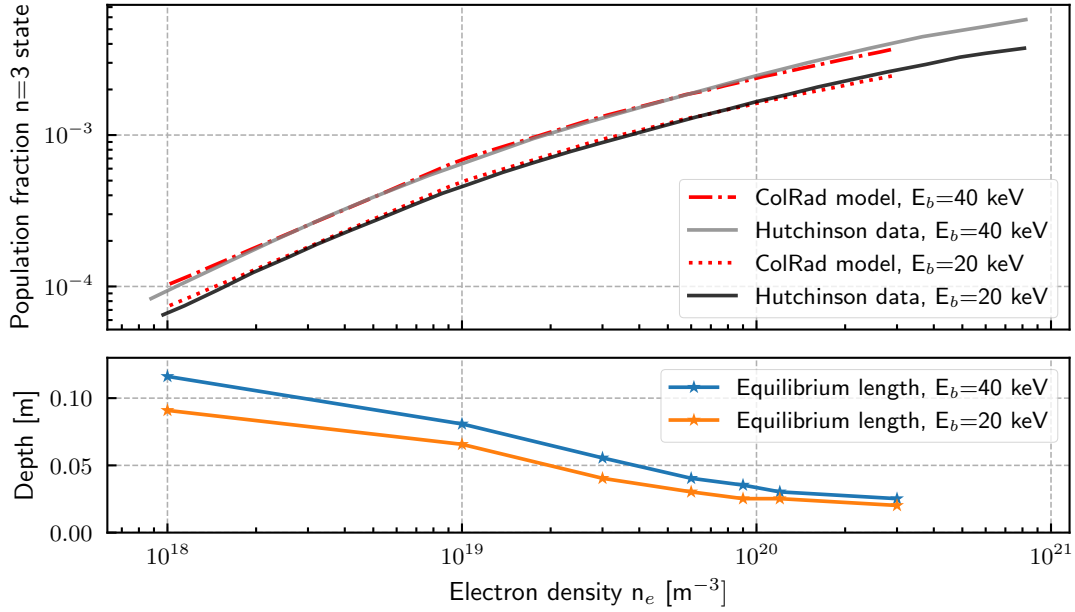
Figure 2. Top: equilibrium neutral beam particle population fraction in n = 3 state as a function of electron density for a electron temperature of 1 keV for two different beam energies E_b. Hutchinson data (black and gray) taken from [14] agrees well with implemented collisional-radiative model (red dashed lines) for both beam energies. Bottom: penetration depth of beam into plasma to reach an equilibrium energy state distribution when assuming a flat density profile for two different beam energies E_b.

3 Halo model

To model the halo formation without employing computationally costly Monte-Carlo techniques a diffusive Ansatz is chosen. The diffusive character of the halo particle transport is based on the fact that multiple CX reactions act as an unbiased 3D random walk process. It is valid to neglect the plasma rotation ($O(1\,\text{km/s})$ [15]) as the thermal velocity of plasma ions, even at the cold plasma edge ($O(100\,\text{km/s})$), is significantly higher. To correctly model the halo diffusion and ionization and to be able to predict the Balmer-α emission, several excited states need to be tracked in a proper collisional-radiative (CR) model. Let the halo particle density be written as a vector

$$\mathbf{n} = (n^{(1)}, \ldots, n^{(i)}, \ldots, n^{(k)}), \tag{3.1}$$

where each component corresponds to the halo density in energy state i (1 being the ground state). In the presented model, 5 excited states are included ($k = 6$). For each energy state there is one partial differential equation, compactly written as

$$\frac{\partial \mathbf{n}}{\partial t} - (\nabla(\mathbf{D}\nabla)) \odot \mathbf{n} = \mathbf{T}_{\text{CR}} \cdot \mathbf{n} + \mathbf{S}_{\text{DCX}} \tag{3.2}$$

where $\mathbf{D}$ are the CX diffusion coefficients for each energy state and $\mathbf{S}_{\text{DCX}}$ are the direct CX reaction rates between beam and plasma into each energy state. The matrix $\mathbf{T}_{\text{CR}}$ effectively contains all collisional-radiative reaction rates and depends on the local plasma parameters (equivalent to equation (2.2) but with differing excitation rates as shown in appendix B). All k diffusion equations

are coupled through the term $\mathbf{T}_{\text{CR}} \cdot \mathbf{n}$. This is understood by realizing that the halo source rate of energy state i not only depends on the direct beam-plasma CX rate into that state but also on excitation and photonic deexcitation neutral rates from lower or higher energy states, respectively. The CX diffusion coefficient for halo neutrals in energy state i is computed as

$$D^{(i)} = \frac{v_{\text{th}}^2}{2 n_{\text{p}} \sum_{j=1}^{j_{\max}} < \sigma_{\text{CX}}^{(i \to j)} v_r >} \tag{3.3}$$

where v_{th} is the thermal velocity of plasma ions and halo neutrals, n_p is the plasma main ion density and $< \sigma_{\text{CX}}^{(i \to j)} v >$ is the Maxwell average of the CX cross section from initial excitation state i to final state j. The averaging needs to be performed over two Maxwellian species interacting with each other and is shown in detail in appendix A. To reduce the complexity of the equation system, 3 assumptions are made: steady state, radially slow varying diffusion coefficients and symmetric, circular diffusion around the gausscil axis. Mathematically this reads as

$$\partial_t \mathbf{n} = 0 \tag{3.4}$$

$$\Delta_z, \Delta_\phi \ll \Delta_r \tag{3.5}$$

$$\partial_r \mathbf{D} \ll \frac{D}{r} \tag{3.6}$$

With the stated assumptions a system of coupled 1D diffusion equations can be written down:

$$-\mathbf{D}\Delta_r \odot \mathbf{n} = \mathbf{T}_{\text{CR}} \cdot \mathbf{n} + \mathbf{S}_{\text{DCX}}. \tag{3.7}$$

These equations are solved numerically on a radial grid at different perpendicular planes along the gausscil axis using finite differences and enforcing the following mixed boundary conditions:

$$\frac{\partial \mathbf{n}(0)}{\partial r} = 0, \ \mathbf{n}(r_{\max}) = 0. \tag{3.8}$$

The first boundary condition is of the Dirichlet type and enforces a gradient of 0 in the center which is required to obtain a continuous profile in cylindrical coordinates. The second boundary condition is of the Neumann type and enforces that the halo density goes to 0 at the radius $r_{\max}$ (set to 0.8 m). Including the ground state, the first 6 energy states are tracked in the CR model.

In figure 3 an example of computed radial halo profiles for a typical beam density profile and two different plasma densities is shown. The plasma profiles were assumed to be flat for these calculations. It can be seen that the radial shape of the ground state halo density and the n = 3 state density are very similar. The halo density has a longer radial fall off length than the beam density which is due to CX diffusion. When increasing the plasma density while keeping the temperature constant one can see that the halo densities on the beam axis increase significantly. At the same time the radial extent of the halo is decreased compared to the lower density case. This is explained by a smaller diffusion coefficient and increased ionization rate coefficients. In conclusion, the final radial shape of the halo is a complex function of the plasma temperature and density profile as well as the beam shape. With increasing plasma density the halo is more strongly confined to the beam region.

Using the halo density in 6 states, it is possible to determine if a single process dominates the equilibrium density in the n = 3 state. Since this translates directly to the measured Balmer-α
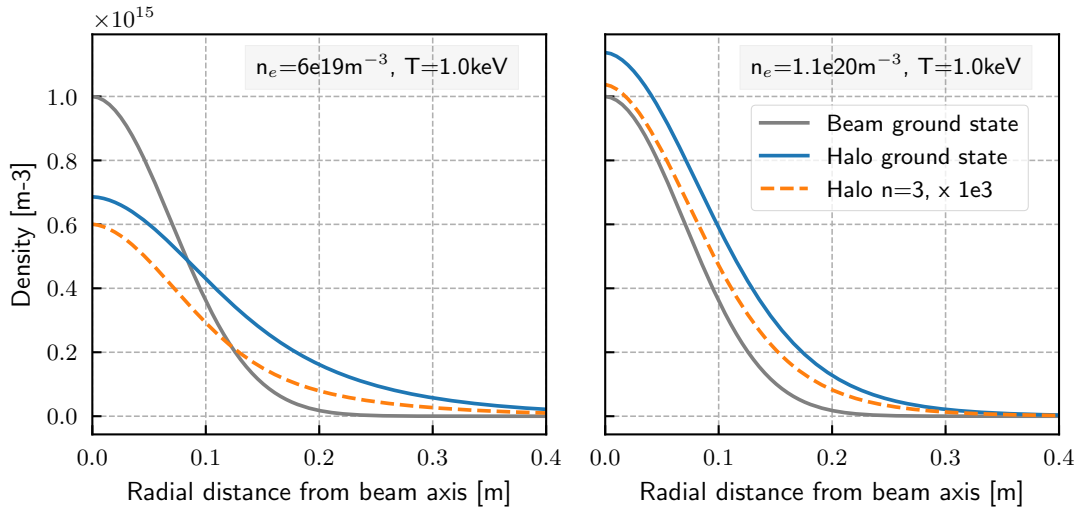
Figure 3. Computed diffusive halo profile as a function of radial distance from the beam axis with shown prescribed beam density as a charge exchange source term and flat plasma profiles. The halo density in the n = 3 state is scaled by a factor of 1e3. The halo density shape follows the beam density shape but extends radially due to diffusion.

light, a single process would open the possiblity of fitting a physical parameter such as the main ion density or temperature directly from the halo emission. In the top of figure 4 all source and loss rates to the halo n = 3 state on the beam axis for a typical single beam discharge (20180821.012) with moderate plasma densities of up to $4.5e19\,\mathrm{m}^{-3}$ are shown. To be able to better evaluate the results, the plasma profiles, the computed ground state beam density as well as the halo density along the beam axis are plotted below. Electron impact excitation and direct beam-plasma charge exchange are the two main source terms of the n = 3 state at all points along the beam meaning over a whole range of plasma parameters. Proton impact excitation and plasma-halo charge exchange reactions only play a minor role in the center of the plasma where the main ion temperature reaches it maximum value. The loss rates consisting of photonic deexcitation and electron and proton impact excitation processes to higher energy states are all of similar magnitude. One must conclude that neither of the collisional processes is dominantly responsible for the equilibrium n = 3 halo density and the measured halo Balmer-α intensity is therefore a function of main ion and electron temperature as well as plasma density. This finding does not necessarily hold for other halo energy states and possibly could be diagnostically exploited if measuring other H lines. The halo emission does, however, allow for a main ion temperature measurement as it is a thermal species with the same temperature as the plasma and the width of the Doppler broadened Balmer-α line is directly proportional to the temperature.

3.1 Effect on beam deposition

The neutral beam injection acts as a plasma fueling source and the beam deposition profile describes where in the plasma and how much of the beam is ionized. When neglecting the halo all beam ionizing reactions (including CX) are counted as local fueling rates. However, CX reactions do
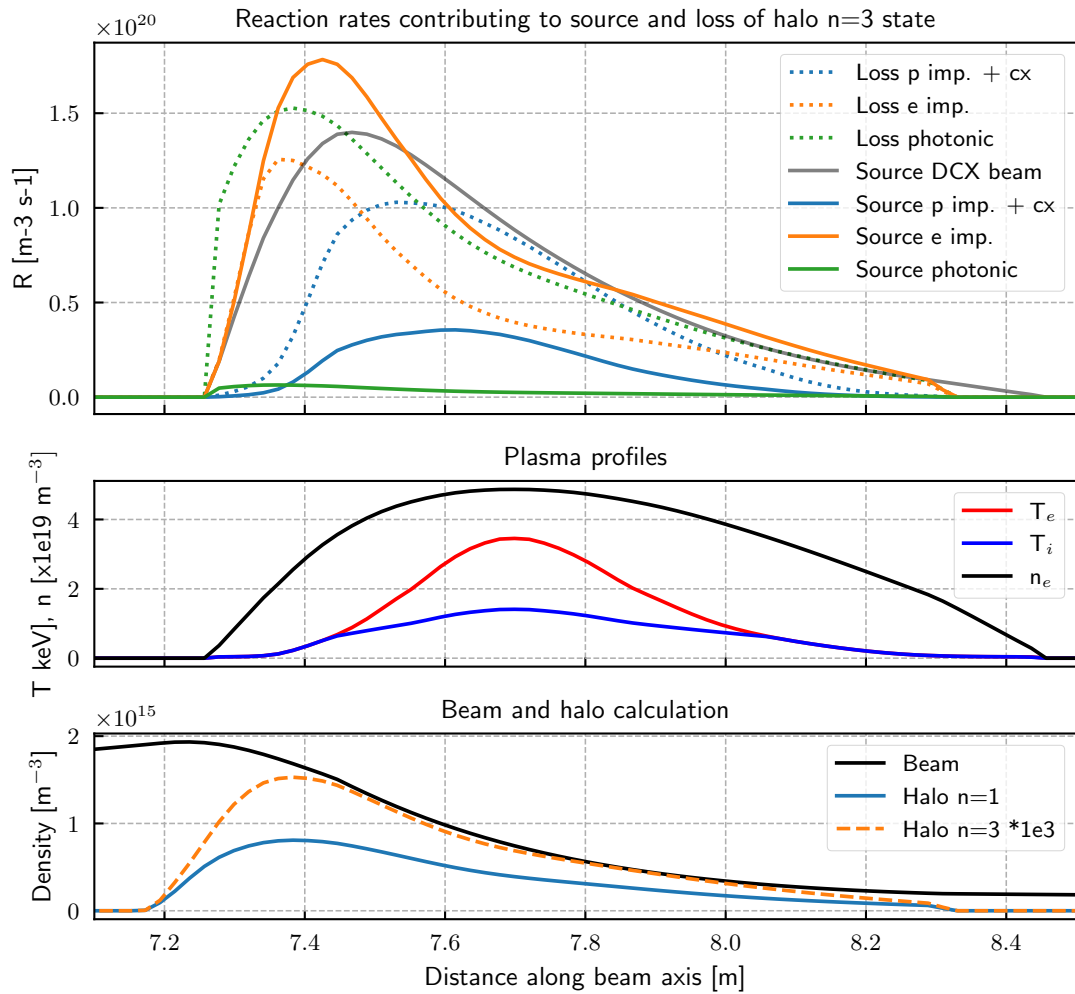
Figure 4. Top: source and loss rates of halo n = 3 state which consist of proton impact, CX, electron impact and photonic deexcitation rates. The rates are computed along the beam axis for a typical single beam discharge (20180821.012). Mid: plasma temperature and density profiles along the beam axis. Bottom: computed beam and halo ground state densities plotted as solid lines and halo n = 3 state density scaled by 1e3 plotted as a dotted line.

not effectively increase the plasma density at the reaction point but create halo particles which will ultimately ionize after a certain diffusion length.

In figure 5 the effect of the halo on the beam particle deposition profile is shown. The binned fueling rate is plotted as a function of the normalized minor radius for two single beam discharges with the same injected power but with different plasma densities. The low (high) density case has a plasma density of $4e19 \, \text{m}^{-3}$ ($6e19 \, \text{m}^{-3}$) over most of the plasma radius. In the low density case, when taking the halo into account, the fueling rate is decreased in the core and increased at the plasma edge. The total particle deposition is reduced by 10%. This effect on the fueling rate is explained by the fact that on average, due to CX diffusion, halo particles diffuse radially outwards before they are ionized. Additionally, due to the diffusion of halo particles out of the plasma volume
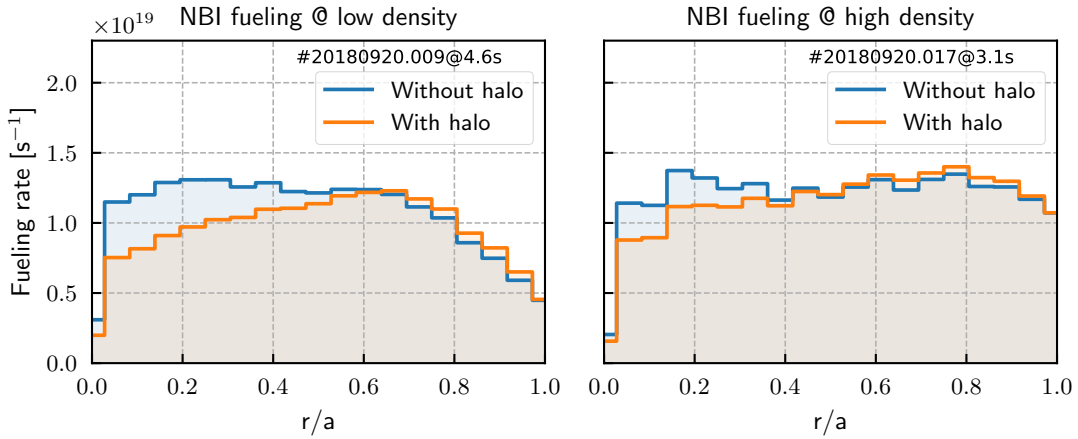
Figure 5. Beam particle deposition profile as a function of normalized minor radius r/a at different plasma densities. The fueling profile neglecting the effect of the halo (beam-plasma CX reactions count as local fueling reactions) is shown in blue and the profile including the effect, thereby representing the fueling profile closer to the physical reality, is shown in orange. Left: low plasma density case ($\approx$4e19 m^{-3}). Right: high plasma density case ($\approx$6e19 m^{-3}).

before ionization the overall particle fueling is smaller than calculated from the naive case ignoring any halo effects. In the high density plasma the particle deposition profile is affected similarly but less pronounced. Due to the high density the CX diffusion is confined to a smaller region around the beam as could already be seen in figure 3 and thereby the fueling profile is less affected. The total deposition rate is reduced by only 3–4% at these plasma parameters.

3.2 Validity of model approximations

At a plasma density of $3 \times 10^{19}\,\mathrm{m}^{-3}$ ($10 \times 10^{19}\,\mathrm{m}^{-3}$) and a ion temperature of 0.5 keV (1 keV) the mean time interval between two CX reactions is approximately 300 ns (100 ns). Therefore, the steady state assumption (equation (3.4)) is valid for all plasmas of interest as the time scales of the atomic and diffusive processes are much shorter than changes in the plasma profiles. It was checked that for W7-X relevant density gradients the CX diffusion coefficient indeed varies slowly (equation (3.6)) except for some cases with a high plasma density at the very edge. There is no general justification to neglect diffusion parallel to the beam axis as stated in equation (3.5). The quality of this assumption can be assessed by comparing the second order radial derivative of the neutral beam and halo density profile to the second order longitudinal (in beam grid coordinates the z axis) derivative.

In figure 6 (top) this ratio is plotted for the halo and beam profile which was shown in figure 4. The Laplace operators were evaluated on the beam axis at different lengths as shown on the x axis. The green area indicates where the radial second order derivative is greater than the second order longitudinal derivative. Except at the plasma edge (r/a > 0.85), the radial Laplace operator of the halo density (orange) is dominant along the beam axis, thereby justifying the assumption that the steady state solution of the halo diffusion equation is mainly determined by the radial part (equation (3.5)). Additionally, the neutral beam profile is a strong driving factor of the final shape of the halo profile as could be seen in figure 3. Its second derivative quantifies the change of the halo
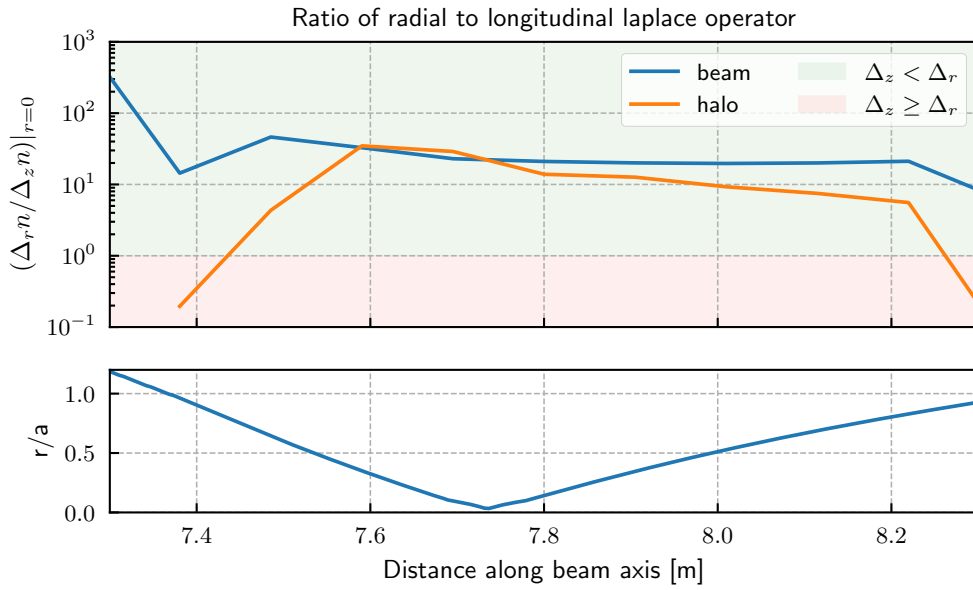
Figure 6. Top: ratio of radial to longitudinal (along axis) second order derivative of the neutral beam (blue) and halo (orange) density evaluated on the beam axis. The calculation was done in a single beam discharge with medium plasma density (20180821.012). Bottom: the normalized, minor plasma radius following the beam axis through the plasma.

source term as it is directly proportional to the beam-plasma CX rate. Along the whole beam axis the Laplace operator of the neutral beam density profile (ratio shown in blue) is strongly dominated by the radial part. Thus, the halo source term varies more strongly radial to the beam axis than along the beam axis. This fact further supports the approximation to solve the halo diffusion equation only in the radial dimension.

4   Verification of modeled neutral densities

The full forward model of the neutral beam injection and halo formation is benchmarked on the validated code FIDASIM [6] in single beam shots. For the benchmark it is ensured that the beam defining parameters (beam power, species fractions, beamlet divergence, focal lengths, source grid size and position) as well as the plasma density and temperature profiles are identical. In both codes the exact same magnetic equilibrium, computed by VMEC [16], is used. The computed $n = 3$ state densities of beam and halo neutrals are compared along a selection of available lines of sight viewing the beam in a roughly horizontal and vertical plane. A detailed description of the CX spectroscopy system installed at W7-X is found in [4].

In figure 7 the modeled neutral beam (top row) and halo (bottom row) densities in the $n = 3$ state are shown and compared to Monte-Carlo calculations one with FIDASIM. The densities are shown along several lines of sight and plotted against the major radius of each point on the line. The beam model agrees very well with FIDASIM regarding the beam shape and the attenuation. As the density of the $n = 3$ state is plotted this additionally indicates that the collisional-radiative model is working as expected. The halo calculation of the same channels achieves a good agreement as well
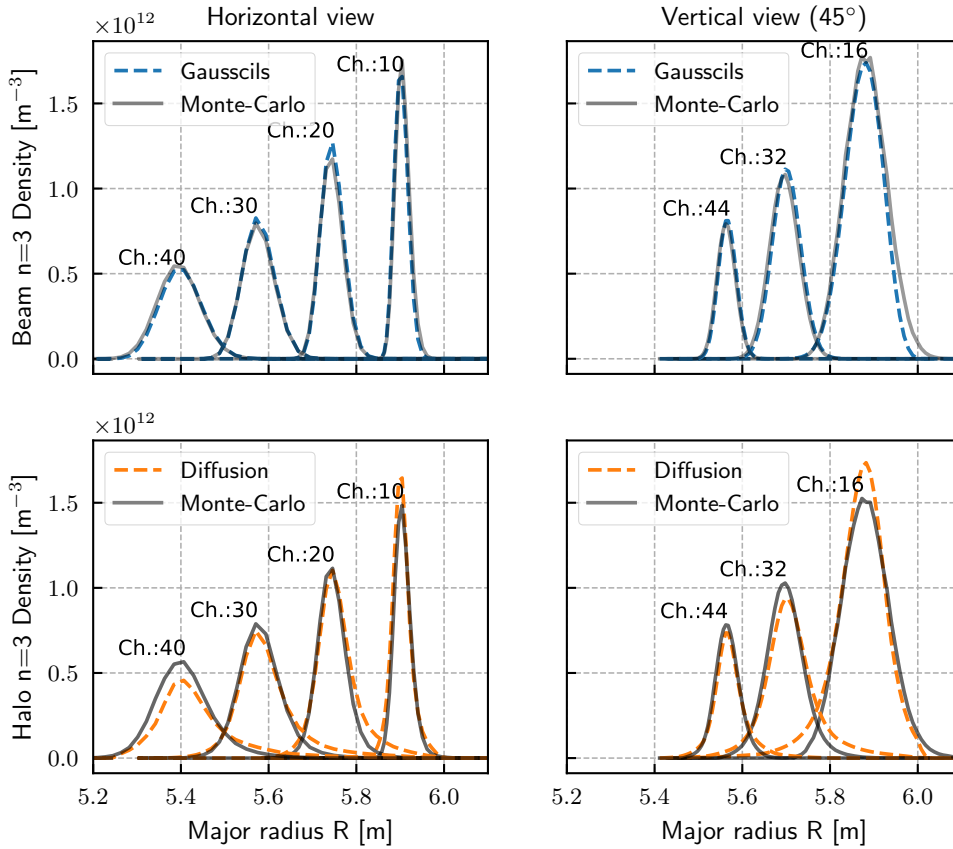
Figure 7. Benchmark of computed beam (Gausscil model) and halo (diffusion model) neutral densities against the Monte-Carlo code FIDASIM [6]. Neutral densities in the n = 3 energy state for the beam (top) and halo (bottom) are plotted along a selection of lines of sight available at W7-X crossing the beam horizontally (left) and more vertically at a 45° angle (right).

with the Monte-Carlo code. In summary it can be stated that the model was verified successfully against the validated code FIDASIM.

5 Balmer-α emission prediction

After computing the beam and halo neutral densities in the n = 3 state the total Balmer-α emission can directly be predicted at any point in the plasma. However to correctly predict the shape of the full measured spectrum one has to take care of Doppler shifts and the motional Stark effect for the beam emission and Doppler broadening ($\propto$ temperature) for the halo emission. The Doppler shift of each beam emission component is straight forward to compute and depends on the beam component energy as well as the angle between the LOS and the beam axis. A slight Doppler broadening due to the effect of a spread of velocity vectors measured with one LOS is inherently incorporated by the Gausscil setup of the beam model.

5.1 Motional stark effect: model and implications

The MSE leads to a splitting of the single Balmer-α line to several, named according to their polarization state, σ and π lines with differing polarization and wavelength [8]. The relative intensity of these lines is modeled by using statistical σ/π ratios from [17]. By taking into account the local magnetic field vector and the LOS geometry, the emitted light intensity and its polarization are calculated and represented as a Stokes vector.

The collection optics of the CX diagnostic include a metal mirror and a coated window (see [4] for details) which lead to a polarisation selective sensitivity. For example, the mirror has different attenuation coefficients for s and p polarisation relative to the surface. Mathematically, the whole collection system is modeled as an arbitrarily rotated, non-ideal polarizer which reads in the Mueller calculus:

$$\mathbf{M}_{\text{mirror}} = \mathbf{R}(-\theta) \frac{1}{2} \begin{bmatrix} 2-c & -c & 0 & 0 \\ -c & 2-c & 0 & 0 \\ 0 & 0 & 0 & 0 \\ 0 & 0 & 0 & 0 \end{bmatrix} \mathbf{R}(\theta) \tag{5.1}$$

The angle θ of the mirror is determined to be $\approx 0°$. The polarizer contrast c was measured to be ≈ 0.2 and describes the fraction of absorbed s-polarized light at the mirror. The used beam emission spectroscopy system does not measure the polarization and consequently only the 0th Stoke vector component after the mirror, S_0', is needed to predict the spectrum.

$$S_0' = \mathbf{S} \cdot \frac{1}{2} \begin{bmatrix} 2-c \\ c\cos 2\theta \\ c\sin 2\theta \\ 0 \end{bmatrix} \tag{5.2}$$

The initial calibration of the system was done with an unpolarized light source and, consequently, is valid for any unpolarized light source in the plasma. The MSE light emitted by the beam is unpolarized only when integrated over the whole space angle. As each LOS only views a small part of the space angle the BES signal is a polarized light source. As a consequence the applied calibration factors need to be corrected by a factor of $\frac{1}{1-0.5c}$ for the BES prediction.

6   First test of the model capabilities — fitting NBI parameters

The full model is tested on a double beam (S7 + S8) discharge with the aim to fit the beam power, divergence, species fractions and beam height (up or down shift in global z direction) as well as corrections to the optical head alignment. The plasma profiles were provided by the Thomson scattering and the CXRS systems. The free parameters were determined with a maximum a-posteriori (MAP) fit including the data of all available lines of sight.

As a reference of the fit quality, achieved with the named free parameters, the full predicted Balmer-α spectrum for a line of sight sensitive to the plasma edge (toroidal view) and the experimental data are shown in figure 8. A very good agreement between the model (red line) and the data (black dotted) is achieved across the whole relevant wavelength range. The predicted halo
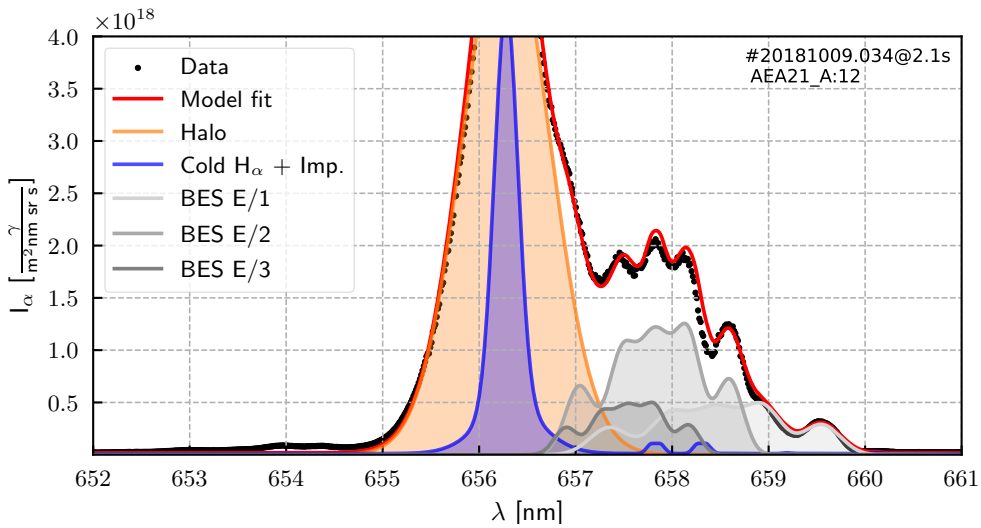
Figure 8. Modeled (red line) and measured (black dotted) Balmer-α emission spectrum in a two beam shot for an A port edge LOS ($\rho \approx 0.8$). Modeled contributions to the full spectrum of halo emission (orange), beam emission(gray) and cold H_α+impurities (blue) are shown as filled graphs.

emission which is marked in orange is centered around the Balmer-α rest wavelength of 656.28 nm as the halo neutrals are a thermal species. Its width and absolute intensity agree almost perfectly with the measured data. The cold H_α emission and the carbon impurity emission (both drawn in blue) are freely fitted with Gaussians at an earlier time point in the discharge, where no beams were active, and then kept constant. The Doppler shifted BES contributions for each injected beam energy component (full, half or third injection energy) summed over both active beam sources are shown in gray tones. Due to the summation over two beams and the MSE splitting the emission of each energy component has a complex spectral shape. After the fit, the shown agreement is also achieved for most of the other lines of sight available in this discharge.

The fitted corrections of the optical head alignment yielded a movement of the lines of sight from 0.2 cm up to 1.2 cm at the beam axes, which is in agreement with results from [4]. The fitting results for the beam parameters are listed in table 2 and compared to the nominal values provided by other diagnostics.

Table 2. Comparison of the nominal NBI parameters to the ones fitted (Bayesian maximum a-posteriori fit) from beam and halo Balmer-α emission data in the double beam discharge 20181009.034.

	Nominal value	MAP fit
Total power S7 (into torus) [MW]	1.8	1.9
Total power S8 (into torus) [MW]	1.7	1.8
Beamlet divergence [°]	0.8	0.75
Power fractions [$p_1/p_2/p_3$]	[0.49 / 0.41 / 0.1]	[0.46 / 0.45 / 0.09]
Upward shift (S7+S8 traversing the plasma)	-	5 cm

The inferred total beam power injected into the plasma differs only slightly by about 5% from the nominal value, which is given by a calibrated neutralized power signal multiplied with
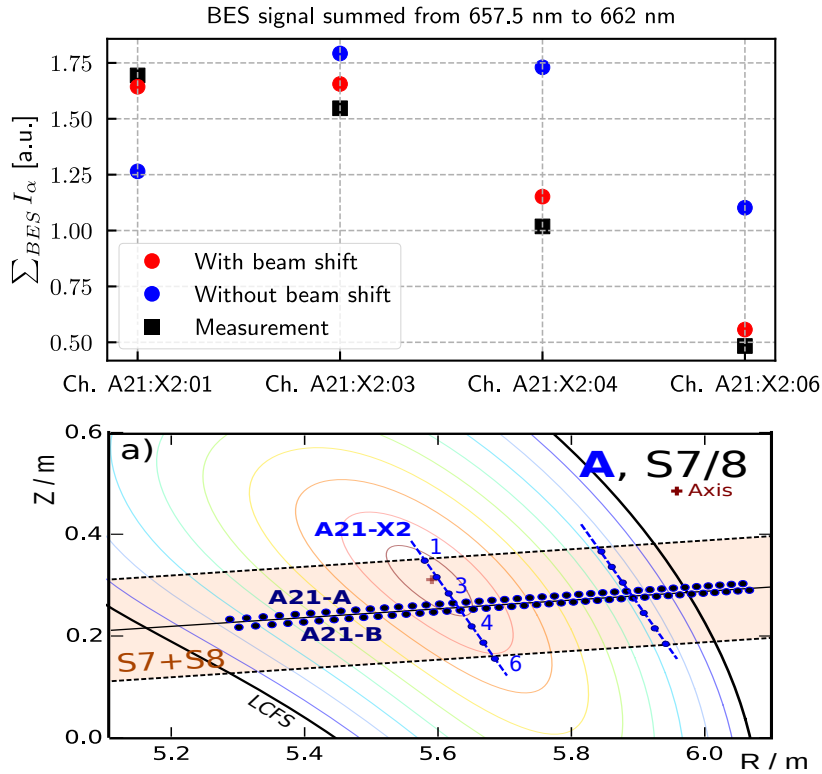
Figure 9. Summed beam emission intensity and beam density for 4 lines of sight (channels) crossing the beam at positions on a line perpendicular to the beam axis and parallel to the global z axis. Top: the Balmer-α emission intensity is summed in a wavelength interval where the beam emission signal dominates (657–662 nm) and plotted for each line of sight. The final fit of the model (red) to the measured data (black dots) requires a shift of about 5 cm upwards along z. Using the nominal beam alignment a good fit (blue) to the measured data cannot be achieved. Bottom: line of sight geometry relative to the beam and the flux surface geometry. The shown A21–X2 channels (1–6) view the beam horizontally and are distributed perpendicular to the beam axis. The bottom figure is reprinted from [4], with the permission of AIP Publishing.

a calculated beam duct factor accounting for scrape off losses at the beam edges on the way to the plasma. The beamlet divergence is fitted to a value of $0.75°$, which is close to the design value of $0.8°$. The inferred species power fractions closely agree with the neutralizer spectroscopy measurements even though its data has not yet been analyzed systematically.

An important result of the modeling effort is the inferred correction of the beam positioning to best fit the measured BES data. It was found that the beams are moved upwards by roughly 5 cm (global z-axis) from the expected position when traversing the plasma. How this can be seen in the data and influences the modeled neutral beam densities, is visualized in figure 9 for a set of lines of sight crossing the beam at a radius of r/a = 0.1 and which, per design, should be distributed symmetrically across the beam (perpendicular to the beam axis) to capture the beam shape. This symmetry can be seen in the bottom plot showing the line of sight geometry relative to the beam and the flux surfaces. The predicted, summed BES signal without including a beam shift, shown in the top plot (blue dots), does not agree with the measured data (black squares). After including a free parameter to be able to shift the beam upwards in the inference process the measured BES data can

be successfully fitted by the model (red dots). It has to be noted that, even though the shown lines of sight have a strong influence on the inferred beam shift, the fit of all free parameters includes the data of all available lines of sight simultaneously. The shown data is just a subset which is best suited to visualize the effect of moving the beam upwards has on the prediction and that doing so enables a significantly improved fit of these channels. The upward shift is most likely explained by the effect of the stray magnetic field on the beam particles before they are neutralized. It has been observed, both, in simulations and during internal shots on the calorimeter, but is still under analysis; the results of which are to be reported later.

7   Conclusion

The Balmer-α light emitted by a neutral beam and its subsequently formed halo contains a large amount of important information ranging from the beam parameters (total power, shape, divergence) to local plasma density and ion temperature. The inference of these parameters from data is a complex and multivariate problem well suited for the application of the Minerva Bayesian analysis framework. The first step in order to employ Bayesian inference is setting up a fast and detailed forward model. In this manuscript the steps undertaken to model the neutral beam attenuation and halo formation at W7-X were described in detail.

To model the radial shape of the beam to sufficient accuracy to achieve a good match to the measured Hα spectrum, it was found that splitting the beam into a grid of 2×5 Gaussian pencil beams (Gausscils) is a good balance between accuracy and computational speed for the W7-X parameters. The chosen grid is adapted to the NBI source grid size ($0.22\,\mathrm{m} \times 0.50\,\mathrm{m}$), yielding Gausscils with a circular shape. A higher number of Gausscils did not improve the modeled beam shape sufficiently, compared to the Monte-Carlo calculation, to justify the increased computational time. Each Gausscil is individually pointed on the as designed horizontal and vertical focal points of the beam. To model the attenuation and emission, a collisional-radiative (ColRad) model is solved stepwise along each Gausscil axis, taking into account the ground state and 5 excited states. The ColRad model was validated on data from an independent publication. It was shown that in order to predict the beam emission in the outer part of the plasma radius, one cannot rely on effective emission coefficients because a certain beam penetration depth is needed to reach an equilibrium in the excited states distribution.

The halo formation is modeled by numerically solving a set of coupled 2D diffusion equations for all tracked energy state while taking into account all collisional radiative processes. The diffusion is assumed to be steady-state and dominantly radial to the beam axis. The predicted neutral densities in the Balmer-α relevant n = 3 state were benchmarked against the validated code FIDASIM [5], and a very good agreement between the two different models was achieved for the modeled beam and halo densities. As the developed model does not rely on Monte-Carlo-techniques at any point, it is orders of magnitudes faster and exhibits no noise in the results.

It could be shown that the local halo Balmer-α emission intensity is dependent on a complex combination of all plasma parameters. The halo emission Doppler broadening, on the other hand, is directly proportional to the ion temperature, which should, in principle, enable the inference of the profile from beam and halo emission data. The effect of the halo on the beam particle deposition profile was quantified for two single beam discharges with different plasma densities. Including

the halo the fueling rate is decreased at normalized radii $\rho < 0.4$ and slightly increased at radii $\rho > 0.5$. This effect is explained by the fact that halo particles, on average, diffuse radially outwards before they are ionized. The diffusion is dominated by CX interactions with the plasma so that any neutral self interaction between halo particles can be ignored. As expected, the impact on the fueling profile becomes less pronounced at a higher plasma density. Consequently, this effect is relevant for particle transport studies at low plasma densities ($\approx 4e19\,\mathrm{m}^{-3}$) but can be ignored at high plasma densities ($\approx 6e19\,\mathrm{m}^{-3}$).

The final step to verify the capabilities of the model was to infer beam parameters in a double beam discharge while taking the plasma profiles as given input parameters. The injected beam power, divergence and species fractions showed a decent agreement with the NBI reference values. The inference result implies that both beams (Q7, Q8) are shifted upwards by about 5 cm when traversing the plasma. After fitting the beam parameters and the optical head alignment a very good agreement between the measurement and the prediction could be achieved for all measurement channels. A subtle detail in the emission modeling process was to correct the calibration factors for the polarized part of the spectrum due to a mirror in the optical path.

In future work the developed beam and halo emission model will be used together with the available data from around 54 lines of sight to study the Bayesian inference capabilities of electron density and ion temperature profiles. The ongoing modeling effort of motional Stark effect measurements at W7-X relies to a great extent on the accurate beam attenuation and emission model. As the developed model is embedded in the rich and flexible Minerva ecosystem it is in principle easily reusable at other or future fusion devices.

Acknowledgments

A   Charge exchange diffusion coefficient

The diffusion coefficient for CX random walks of neutral hydrogen in energy state i can be written as:

$$D^{(i)} = \frac{(\Delta x)^2}{2\Delta t} = \frac{\lambda_{\mathrm{CX}}^{(i)} <v>}{2} \tag{A.1}$$

$$<v> = \sqrt{8kT_i/(\pi m_p)} \tag{A.2}$$

Here $\lambda_{\mathrm{CX}}^{(j)}$ is the mean free path of a neutral in energy state j if only taking CX into account. Maxwell averaged mean free path:

$$\lambda_{\mathrm{CX}} = \frac{<v_1>}{n_{\mathrm{ion}} <\sigma_{\mathrm{CX}} v>} \tag{A.3}$$

The computed diffusion coefficient and mean free path for energy states 1 and 3 and for different plasma densities is shown in figure 10.
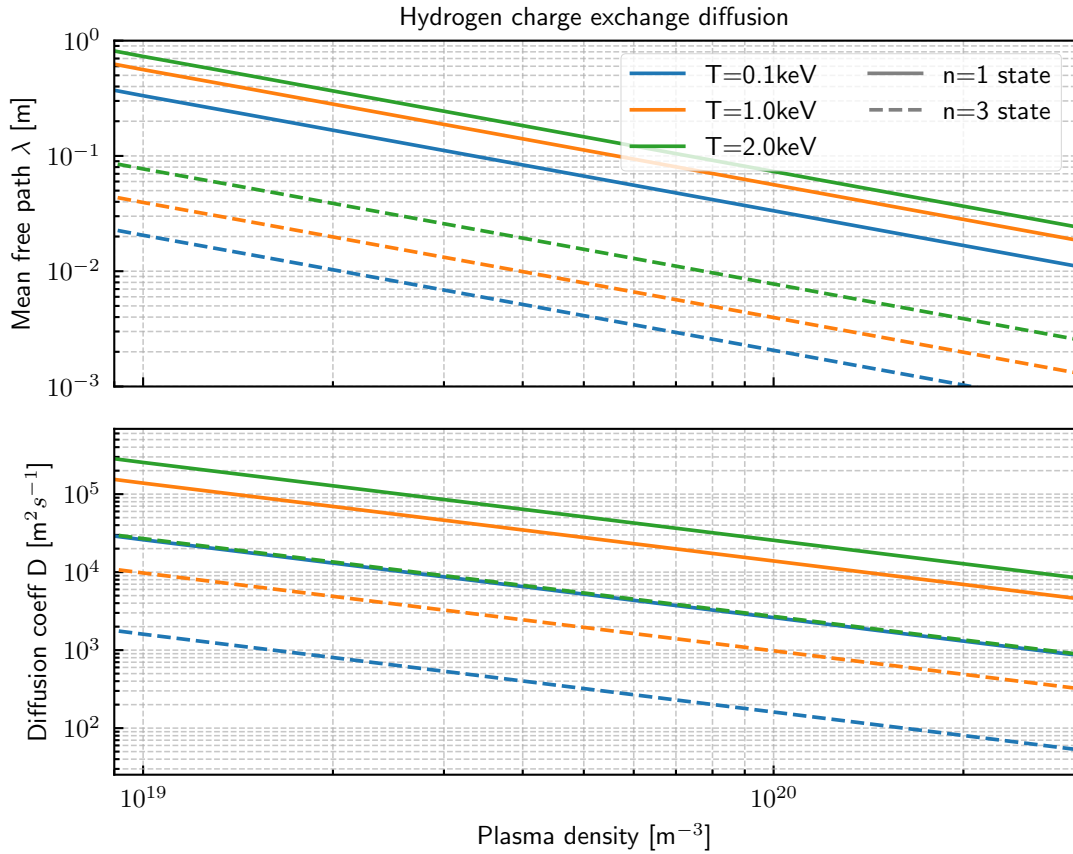
Figure 10. Mean free path and diffusion coefficient of thermal hydrogen neutrals in a thermal hydrogen plasma when taking only charge exchange reactions into account.

The cross section average of two Maxwellian distributed species (plasma and halo neutrals) can be computed using center of mass coordinates:

$$< \sigma v > = \int \int d\vec{v}_1 d\vec{v}_2 \sigma(v_r) v_r f_1(\vec{v}_1) f_2(\vec{v}_2) \tag{A.4}$$

$$= C_1 C_2 \int \int d\vec{v}_r d\vec{V}_c \sigma(v_r) v_r e^{-(\beta/2)(M_{12}V_c^2 + m_r v_r^2)}$$

Integration over center of mass velocity V_c multiplied with C_1 yields 1. Transformation to spherical coordinates as problem is symmetric in ϕ, θ:

$$< \sigma v > = \left(\frac{m_r}{kT2\pi}\right)^{3/2} 4\pi \int dv_r \sigma(v_r) v_r^3 e^{-\frac{m_r v_r^2}{2kT}}$$

$$= 4\pi \int dv_r \ \sigma(v_r) v_r f_{\text{Maxwell}}(v_r, m_r) \tag{A.5}$$

$$m_r = \frac{m_1 m_2}{m_1 + m_2} \tag{A.6}$$

B Collisional-radiative processes

In the collisional-radiative (CR) models for the beam and the halo presented in this paper all photonic, proton impact, electron impact and charge exchange rates of excitation and deexcitation are written in a matrix form which then acts on a vector containing the neutral density in each excitation state.

$$
T_{\mathrm{CR}} = T_{\mathrm{CR}}(T_e, T_i, n_e) = \begin{bmatrix}
-L_1 & A_{21} & A_{31} & . & A_{k1} \\
E_{12} & -L_2 & A_{32} & . & A_{k2} \\
E_{13} & E_{23} & -L_3 & . & . \\
. & . & . & . & A_{ki} \\
E_{1k} & E_{2k} & . & E_{jk} & -L_k
\end{bmatrix} \tag{B.1}
$$

Here A are the Einstein coefficients for spontaneous deexcitation, E_{ij} the collisional excitation rates and L_i the summed loss rate to state i.

Rates beam model. With the electron density (n_e), the main ion density (n_i), the electron impact excitation cross section (σ_e), the proton impact excitation cross section (σ_p) and the CX cross section (σ_{CX}) the excitation and loss rates can be written as:

$$
E_{ij} = n_e <\sigma_e^{(ij)} v> + n_i <\sigma_p^{(ij)} v> \tag{B.2}
$$

$$
I_i = n_e \left(<\sigma_e^{(iI)} v> + <\sigma_p^{(iI)} v> + \sum_{j=1}^{k} <\sigma_{\mathrm{CX}}^{(ij)} v> \right) \tag{B.3}
$$

$$
L_i = I_i + \sum_{m=i+1}^{k} E_{im} + \sum_{m=1}^{i-1} A_{im} \tag{B.4}
$$

where I are the ionization rates. The Maxwell average of the cross sections $<\sigma_p v>$ is dominated by the beam particle velocity as the beam particles are much faster than the thermal plasma ions. Therefore, all beam CR rates are only weakly dependent on the electron and ion temperature.

Rates halo model. These are identical to the ones in the beam model except that the excitation rates additionally include the additional CX rates.

$$
E_{ij} = n_e <\sigma_e^{(ij)} v> + n_i \left(<\sigma_p^{(ij)} v> + <\sigma_{\mathrm{cx}}^{(ij)} v> \right) \tag{B.5}
$$

The Maxwell averages of the cross sections $<\sigma_p v>$ and $<\sigma_{\mathrm{CX}} v>$ need to be performed over two Maxwellian species as described in equation (A.4) and is therefore dependent on the plasma ion temperature.

References

[1] J. Svensson and A. Werner, *Large Scale Bayesian Data Analysis for Nuclear Fusion Experiments*, *IEEE Int. Symp. Intell. Signal Process.* **2007** (2007) 1.

[2] P. McNeely et al., *Current status of the neutral beam heating system of w7-x*, in *Proceedings of the 27th Symposium On Fusion Technology (SOFT-27)*, Liège, Belgium (2012) [*Fusion Eng. Des.* **88** (2013) 1034].

[3] W. Mandl, R.C. Wolf, M.G. von Hellermann and H.P. Summers, *Beam emission spectroscopy as a comprehensive plasma diagnostic tool*, *Plasma Phys. Control. Fusion* **35** (1993) 1373.

[4] O.P. Ford et al., *Charge exchange recombination spectroscopy at wendelstein 7-x*, *Rev. Sci. Instrum.* **91** (2020) 023507.

[5] L. Stagner et al., *FIDASIM: A Neutral Beam and Fast-ion Diagnostic Modeling Suite*, https://doi.org/10.5281/zenodo.1341369.

[6] B. Geiger et al., *Progress in modelling fast-ion d-alpha spectra and neutral particle analyzer fluxes using FIDASIM*, *Plasma Phys. Control. Fusion* **62** (2020) 105008.

[7] W.W. Heidbrink, D. Liu, Y. Luo, E. Ruskov and B. Geiger, *A Code that Simulates Fast-Ion Dα and Neutral Particle Measurements*, *Commun. Comput. Phys.* **10** (2011) 716.

[8] F.M. Levinton, *The motional stark effect: Overview and future development (invited)*, *Rev. Sci. Instrum.* **70** (1999) 810.

[9] S.R. Haskey et al., *Active spectroscopy measurements of the deuterium temperature, rotation, and density from the core to scrape off layer on the DIII-d tokamak (invited)*, *Rev. Sci. Instrum.* **89** (2018) 10D110.

[10] R.M. McDermott et al., *Evaluation of impurity densities from charge exchange recombination spectroscopy measurements at ASDEX upgrade*, *Plasma Phys. Control. Fusion* **60** (2018) 095007.

[11] S.A. Lazerson et al., *Validation of the BEAMS3d neutral beam deposition model on wendelstein 7-x*, *Nucl. Fusion* **60** (2020) 076020.

[12] A. Spanier et al., *Performance of the first neutral beam injector at the wendelstein 7-x stellarator*, *Fusion Eng. Des.* **163** (2021) 112115.

[13] S. Kwak, J. Svensson, M. Brix and Y.-C. Ghim, *Bayesian electron density inference from JET lithium beam emission spectra using gaussian processes*, *Nucl. Fusion* **57** (2017) 036017.

[14] I.H. Hutchinson, *Excited-state populations in neutral beam emission*, *Plasma Phys. Control. Fusion* **44** (2001) 71.

[15] J. Alonso et al., *Plasma flow measurements based on charge exchange recombination spectroscopy in the wendelstein 7-x stellarator*, *Nucl. Fusion* **62** (2022) 106005.

[16] S. Hirshman, W. van RIJ and P. Merkel, *Three-dimensional free boundary calculations using a spectral Green's function method*, *Comput. Phys. Commun.* **43** (1986) 143.

[17] E.U. Condon and G.H. Shortley, *The theory of atomic spectra*, Cambridge University Press (1935).